Complex mixture of organic matter in a xenolithic clast from the Zag meteorite revealed by coordinated analyses using AFM-IR, NanoSIMS and STXM/XANES

Yoko Kebukawa, Jérémie Mathurin, Dartois E., Ferenc Borondics, Ariane Deniset-Besseau, Jean Duprat, Laurent Remusat, Takaaki Noguchi, Akira Miyake, Yohei Igami, et al.

Complex mixture of organic matter in the xenolithic clast from the Zag meteorite revealed by coordinated analyses using AFM-IR, NanoSIMS and STXM/XANES

Yoko Kebukawa[1]*, Jérémie Mathurin[2], Emmanuel Dartois[3], Alexandre Dazzi[4], Ariane Deniset-Besseau[4], Jean Duprat[5], Laurent Remusat[5], Takaaki Noguchi[6], Akira Miyake[6], Yohei Igami[6], Maximilien Verdier Paoletti[5], Michael E. Zolensky[7], Cécile Engrand[2], Christophe Sandt[8], Ferenc Borondics[8], Shohei Yamashita[9], Daisuke Wakabayashi[9], Yasuo Takeichi[9†], Yoshio Takahashi[10]

*Corresponding author: kebukawa@ynu.ac.jp

[1] Department of Chemistry and Life Science, Yokohama National University, 79-5 Tokiwadai, Hodogaya-ku, Yokohama 240-8501, Japan

[2] Université Paris-Saclay, CNRS/IN2P3, IJCLab, 91405 Orsay, France

[3] Institut des Sciences Moléculaires d'Orsay, UMR8214, CNRS, Université Paris-Saclay, 91405 Orsay, France

[4] Institut de Chimie Physique, UMR 8000, Université Paris-Saclay, CNRS, 91405, Orsay, France

[5] Institut de Minéralogie, de Physique des Matériaux et de Cosmochimie, CNRS UMR 7590 - Sorbonne Université -Museum National d'Histoire Naturelle, 57 rue Cuvier 75005 Paris, France

[6] Division of Earth and Planetary Sciences, Kyoto University, Kitashirakawaoiwake-cho, Sakyo-ku, Kyoto 606-8502, Japan

[7] Astromaterial Research and Exploration Science, NASA Johnson Space Center, 2101 NASA Parkway, Houston, TX 77058, USA

[8] Synchrotron SOLEIL, L'Orme des Merisiers, BP48 Saint Aubin, 91192 Gif-sur-Yvette Cedex, France

[9] Institute of Materials Structure Science, High-Energy Accelerator Research Organization, 1-1 Oho, Tsukuba, Ibaraki 305-0801, Japan

[10] Department of Earth and Planetary Science, The University of Tokyo, Hongo, Bunkyo-ku, Tokyo 113-0033, Japan

[†] Current address: Department of Applied Physics, Osaka University, 2-1 Yamadaoka, Suita, Osaka 565-0871, Japan

Abstract

Primitive carbonaceous xenolithic clasts found in sturdy metamorphosed meteorites often provide opportunities to reach labile volatile-rich materials which are easily destroyed during atmospheric entry and materials which we do not have sampled as individual meteorites. Among them, a xenolithic carbonaceous clast in the Zag ordinary chondrite has been providing us with the opportunity to analyze a possible sample from D/P-type asteroids. Here we performed a new suite of coordinated analyses of organic matter in the Zag clast using the state-of-the-art AFM-IR combined with NanoSIMS, STXM/XANES, Raman, and (S)TEM on adjacent ultramicrotomed thin sections from a single sample grain. We successfully demonstrated the practicality of coordinated analyses using AFM-IR, Raman and NanoSIMS on the same sample area, as well as STXM/XANES on adjacent (and nearly identical) thin sections to those used for AFM-IR. The AFM-IR map and STXM maps provided consistent and complementary results. We found that at least two types of organics were closely mixed in this specimen. One was deuterium-rich, C=O rich organics with likely smaller aromatic domains, possibly originating in relatively oxidized environments from D-rich precursors. The other type was less deuterium-rich, but aromatic-rich organics, possibly produced in relatively reduced and higher temperature environments with less deuterium-rich precursors. These characteristics point to complex mixtures of materials with different origins and sampling a wide heliocentric range of the Solar System before accretion in the parent body of the clast.

Keywords

meteorite, chondrite, asteroid, organic matter

1. Introduction

Primitive planetary materials are key to understanding the origin and evolution of our Solar System. A wide variety of organic compounds are often found in these materials, dominated in mass by a complex macromolecular organic matter, also known as insoluble organic matter (IOM). The organic matter has formed and evolved at various stages of the solar system evolution, including the precursor molecular clouds, protoplanetary disk, and subsequent small bodies — some of them probably becoming raw materials for the origin of life.

However, the primitive and organic-rich small bodies are also usually volatile-rich and are easily destroyed when they enter the Earth's atmosphere, and thus it is rare to collect these as meteorites. Such fragile bodies are also easily pulverized when they collide with other small bodies. However, if a primitive and fragile body collides with a firm body and fragments are preserved in it, the fragile material may be able to reach the Earth as a xenolithic clast protected inside a sturdy meteorite which is mechanically robust against atmospheric-entry alteration. Carbonaceous chondrite-like clasts are often found in various meteorites including chondrites, ureilites, howardites (e.g., Brearley, 1990; Brearley and Prinz, 1992; Zolensky et al., 1992; Zolensky et al., 1996; Gounelle et al., 2003; Briani et al., 2009; Rubin and Bottke, 2009; Bonal et al., 2010a; Bonal et al., 2010b; Briani et al., 2012; Kebukawa et al., 2017; Patzek et al., 2018; Nittler et al., 2019; Patzek et al., 2020). A primitive xenolithic clast in the Zag H3-6 ordinary chondrite is significantly rich in carbon, and shows molecular structure and isotopic characteristics of organic matter different from the typical carbonaceous chondrite groups (Rubin et al., 2002; Zolensky et al., 2017; Kebukawa et al., 2019a; Kebukawa et al., 2020). We have proposed that the Zag clast originated from the outer solar system and was subsequently incorporated into the ordinary chondrite parent body located in the inner solar system (Kebukawa et al. 2019a, 2020). However, the detailed history of organic matter in the clast is not well understood.

Classical methods to analyze trace organics in meteorites are solvent extraction and acid demineralization. The spatial and textural contexts, however, are lost by these methods. To understand chemical and physical processes that may have affected organic matter, fine-scale

observations of planetary materials are mandatory, including characterization of morphology and spatial relationship between organics and minerals. Scanning transmission X-ray microscopy/X-ray absorption near-edge structure (STXM/XANES) is a well-established technique for the microscopic characterization of organic matter in meteorites (Le Guillou et al., 2014; e.g., Kebukawa et al., 2017; Vinogradoff et al., 2017) and other astromaterials including cometary particles and micrometeorites (Cody et al., 2008; De Gregorio et al., 2011; Noguchi et al., 2017; Yabuta et al., 2017). Alternatively, atomic force microscope-based infrared spectroscopy based techniques such as AFM-IR (Kebukawa et al., 2019b; Mathurin et al., 2019; Phan et al., 2022) and s-SNOM (Dominguez et al., 2014; Yesiltas et al., 2021; Young et al., 2022) have recently begun to be employed to characterize astromaterials. These methods provide similar spatial resolution at the scale of tens of nanometers, both detect organic functional groups although STXM/XANES also allows the determination of oxidation states of e.g., Fe, and AFM-IR provides mineral signatures. In addition, nanoscale secondary ion mass spectrometry (NanoSIMS) produces isotopic signatures at comparable spatial resolution. These microscopic methods provide complementary information of functional groups and isotopic ratios to elucidate the origins and evolutional history of organic matter which is heterogeneously mixed in the fine-scale matrix of astromaterials. Thus, the same sample areas are often analyzed by both STXM/XANES and NanoSIMS (De Gregorio et al., 2010; De Gregorio et al., 2013; Kebukawa et al., 2019a; Kebukawa et al., 2020; Kebukawa et al., 2021b), and such coordinated analysis, including AFM-IR, is also desired.

Here we report coordinated analysis using AFM-IR and NanoSIMS on the same area of the unique organic-rich clast in the Zag meteorite. In addition, STXM/XANES, Raman, synchrotron-based FTIR microspectroscopy, and (scanning) transmission electron microscopy ((S)TEM) provide insight into the origins and evolutional history of the organic matter in the Zag clast.

2. Methods

2.1. Sample preparation with sulfur-embedded ultramicrotomy

The ultramicrotomy method allows us to prepare several nearly-identical sections for different analytical techniques, e.g., AFM-IR and STXM/XANES. The sulfur-embedding method was

118 employed to avoid epoxy resin which causes severe contamination for organic analysis. A small
119 particle of the Zag clast was embedded in molten sulfur for ultramicrotomed thin sections
120 (Noguchi et al., 2020). About 100 nm-thick sections were prepared with a LEICA
121 ultramicrotome using a DIATOME diamond knife, then transferred to copper TEM grids with
122 silicon monoxide supporting films (Pelco® Cu 300 mesh grid) for STXM/XANES and to a CVD
123 diamond window for AFM-IR and NanoSIMS analyses. After ultramicrotomy, the sections were
124 immediately heated gently at 80°C for 12 hours to sublimate the sulfur. We also prepared
125 approximately 100 nm-thick ultrathin sections in Embed 812 epoxy. Both sulfur-embedded and
126 epoxy-embedded ultrathin sections were placed on copper grids with carbon supporting film
127 (LAAD® Cu 100 mesh grid), and were investigated by (S)TEM.
128
129 **2.2. STXM/XANES**
130
131 Carbon-edge X-ray absorption near-edge structure (C-XANES) analyses were performed using
132 the scanning transmission X-ray microscope (STXM) at BL19A, Photon Factory, High-Energy
133 Accelerator Research Organization (KEK) (Takeichi et al., 2016). The elemental maps were
134 obtained by acquiring pairs of images with 0.1 μm steps per pixel below (I_b) and on the
135 absorption edges (I_a), namely at 280 and 292 eV for C *K*-edge, 525 eV and 539 eV for O *K*-edge,
136 and 705 eV and 709 eV for Fe L_3-edge, and then taking the $-\ln(I_a/I_b)$ for each pixel. Spectral
137 image stacks at the C *K*-edge (280-320 eV) were acquired with energy step sizes of 0.1 eV in the
138 fine structure region and 0.5-1.0 eV in the pre- and post-fine structure regions, with a dwell time
139 of 3 ms, and with 0.1 μm steps per pixel. C-XANES spectra from the region-of-interests (ROIs)
140 were extracted and submitted to three-point smoothing to reduce noise, subtracted baselines were
141 fit by linear approximations at 280-283 eV, then normalized with the optical density at 295.5 eV.
142 The spectral component maps were obtained from images at 285.3 eV, 288.7 eV, and 290.5 eV
143 by subtracting an image at 283.0 eV, 289.2 eV, and 289.7 eV, respectively, after converting –
144 $\ln(I/I_0)$, where I is the spectral signal from ROI and I_0 is the spectral signal from blank area
145 adjacent to the ROI, for each image. We used the software aXis2000
146 (http://unicorn.mcmaster.ca/aXis2000.html) for STXM/XANES data analysis, and Adobe
147 Photoshop for generating RGB images.
148

2.3. Nanoscale IR spectroscopy (AFM-IR)

IR maps and spectra at the tens of nanometer scale were obtained using AFM-IR, a technique combining an Atomic Force Microscope (AFM) to a tunable Infrared (IR) laser. An AFM probe detects the photo-thermal expansion that occurs in the sample after IR absorption of the material located just under the AFM tip (Dazzi et al., 2005). AFM-IR was used in tapping mode: in this mode, the photo-thermal expansion is detected using a non-linear interaction (Mathurin et al., 2019; Mathurin et al., 2020). The spatial resolution depends on the nanometer-sized AFM tip radius, overcoming by orders of magnitude the diffraction limit of conventional IR microscopy.

The AFM-IR system was a NanoIR2 from Anasys Instrument (Bruker). The system was coupled to a multi-chip Quantum Cascade Laser (QCL, Daylight Solutions) source covering the mid-IR range from 900 cm^{-1} up to 1960 cm^{-1}. An Au-coated silicon AFM tip was used (Budget sensors, tap 300). IR maps (AFM images of 50 μm × 50 μm, 1000 × 1000 pixels) were acquired at fixed tuned laser wavenumbers: 1020, 1500, 1600 and 1740 cm^{-1}, corresponding to the absorptions of silicates, carbonates, aromatic carbon and carbonyl chemical groups, respectively. The IR mapping acquisitions were made using a 0.05 Hz scan rate with a laser power of 10.33% of the QCL chip, a repetition rate of 1355 kHz and a pulse width of 160 ns.

These maps were combined in a composite three color RGB image (1020 cm^{-1}, green; 1500 cm^{-1}, blue; 1740 cm^{-1} red). Before combining the maps, they were corrected for minor AFM stripping by interpolation, realigned on the 1020 cm^{-1} map using their topographic AFM maps, and slightly smoothed using a 5 pixels kernel. To maximize the contrast between bands with different intrinsic intensities in the composite, the intensity of each image recorded at a given wavenumber was first normalized to its maximum intensity over the entire map before combining them.

Spectra spanning the full QCL multi-chip spectral range were also recorded along the line shown in **Fig. 2c**. Spectra presented in this study were acquired at a 1 cm^{-1} spectral resolution using the same laser parameter as IR mappings spectra and are averages of 8 individual spectra taking on the same position.

2.4. Synchrotron Radiation Infrared microspectroscopy (SR-μFTIR)

Infrared measurements were performed on the SMIS beam line at the SOLEIL synchrotron. The synchrotron IR beam was coupled to a Continuum infrared microscope (ThermoFisher Scientific) to record hyperspectral maps from 750 cm^{-1} to 5000 cm^{-1}. The infrared spot size was optimized close to the diffraction limit, with an IR beam 8 μm × 8 μm confocal aperture. We used a spatial sampling measured with a 4 μm step allowing the map to cover the entire fragment. Each spectrum in the map was recorded at 8 cm^{-1} spectral resolution and is the average of 64 individual scans.

2.5. Raman

A Raman spectral map was acquired with a Thermo Fisher DXR spectrometer, using a laser source at 532 nm at a power of ~300 μW on the sample to prevent sample alteration. The 11 μm × 26 μm map located on the central region of the sample was recorded with a ×100/0.9 numerical aperture objective at a sampling step of 1 μm. Two scans with integration times of 10 s each were co-added for each spectrum. The spot size of the Raman spectra was of the order of ~1 μm, i.e. lower than that of conventional IR spectra.

The Raman spectra were fitted as described in Dartois et al. (2018). The Raman spectra are analysed using a classical Raman band fitting procedure decomposition contributing to the D and G bands, consisting of the deconvolution of five sub-bands (e.g., Sadezky et al. 2005; Kouketsu et al. 2014), then grouped into two main contributions ("D" = D1 + D2 + D4, in green and "G" = D3 + G in red, shown in **Fig. 3**).

2.6. NanoSIMS

The hydrogen isotopic measurements were performed by scanning ion imaging with the NanoSIMS instrument at MNHN in Paris. The NanoSIMS isotopic images were acquired with a 16 keV Cs^+ primary ion beam with a probe dwell time of 1 ms per pixel. The Cs^+ primary beam

was set at ~12 pA, resulting in a probe diameter of ~ 250 nm. The H^- and D^- secondary ions were filtered in the mass spectrometer with a mass resolving power of 3000. Images of H^-, D^- were simultaneously recorded on 2 individual electron multipliers (EM) as a stack of about 80 frames over 20 µm × 20 µm areas with 256 × 256 pixels per frame. We imaged 2 zones located on upper and middle part of the sample (see **Fig. 2b**).

In order to avoid charging effects, the sample was coated with 20 nm of gold prior to introduction into the NanoSIMS instrument. In order to reduce the transition time necessary to reach the sputtering equilibrium regime, each imaged area was implanted for about 10 minutes with a primary ion beam of 250 pA over 30 µm × 30 µm areas centered on the region analyzed.

The instrumental mass fractionation was measured before and after sample analyses using terrestrial standards (Type III Kerogen, Orgueil IOM and dedicated organic polymer thin films with a large range of D/H ratios (Bardin et al., 2015)).

The NanoSIMS images were processed using the LIMAGE software developed by Larry Nittler (Carnegie Institution in Washington DC, currently Arizona State University), ImageJ (https://imagej.nih.gov/ij/) and IDL software. We performed dead time correction (44 ns) on all data and frame alignment following the usual procedures. The frames were subsequently summed and a mask was applied with a minimum threshold set at 1500 cts of H- ions.

The H^- images were aligned to the AFM topographic images using the structures located on the right border of the sample. The same alignment was then used for the D^- image and resulting D/H images were produced using a smoothing kernel of 5 × 5 pixels to take account of the size of the Cs^+ probe and reduce statistical fluctuations.

2.7. TEM

A field emission (S)TEM JEOL JEM-3200FSK at Kyushu University operating at 300 kV equipped with an Ω energy filter was used for observation of phases in the ultrathin sections. Another field emission (S)TEM JEOL JEM-2100F operating at 200 kV at Kyoto University was

used for additional (S)TEM observation and quantitative energy dispersive spectrometer (EDS) analysis of minerals in the ultrathin sections. The ζ-factor method was used for quantitative analysis (Watanabe and Williams, 2006). We used the ζ-factors determined by JEOL Co. Ltd. We confirmed that their ζ-factors were applicable to obtain the chemical compositions of minerals. EDS analysis of minerals in an ultramicrotomed section of Zag was also performed using TEM JEOL JEM-2000FXII operating at 200 kV at Ibaraki University. The Cliff-Lorimer method was used for quantitative analysis. K factors were determined experimentally using many mineral standards.

3. Results

3.1. STXM/C-XANES

The STXM carbon map shows that sub-micrometer organic particles are spread over the section of the Zag clast (**Fig. 1b**). Some particles show a well-defined carbon absorption (e.g., ROI#1 and #2 in **Fig. 1b**), and some are not well distinguished and rather diffuse into the mineral matrix (e.g., ROI#6 in **Fig. 1b**). The molecular structures revealed by C-XANES show common features with large variations in their relative intensities (**Fig. 1e**). Common features are a dominant peak at 285.3 eV due to aromatic carbon, peaks at 288.7 eV due to C(=O)O (carboxy/ester) and at 290.5 eV due to carbonate (that could be both organic and inorganic), a small peak at 286.7 eV due to C=O (ketone), and a shoulder at ~287.7 eV due to aliphatic carbon. The component map (**Fig. 1d**) shows heterogeneities in the intensities of aromatic (285.3 eV) and C(=O)O (288.7 eV). The well-defined particles, e.g., ROI#1 and #2 in **Fig. 1b**, tend to have a larger aromatic peak (285.3 eV) and a smaller carbonate peak (290.5 eV) compared to the average spectra of the entire analyzed area (the red square in **Fig. 1b**). While, ROIs#3, #4, and #6 showed less-aromatic nature. These features generally agree with that of unheated carbonaceous chondrites (e.g., Le Guillou et al., 2014). The spectral component map of the Zag clast (**Fig. 1d**) show that aromatic carbon (285.3 eV) and carbonate (290.5 eV) are distributed separately as <~1 μm spots, while C(=O)O (288.7 eV) is distributed as smaller spots or spread all over within a diffuse organic matter component. The component map is consistent with C-XANES spectra extracted from ROI#1 and #2 which are dominated by aromatic carbon (285.3 eV). It should be noted that 287.5-289 eV region is easily affected by contamination and other artifacts, particularly with

regions containing small amounts of carbon. Thus, the spreading of C(=O)O could be contamination/artifacts. However, C-rich regions as shown by arrows in **Fig. 1b** are likely less affected by these artifacts.

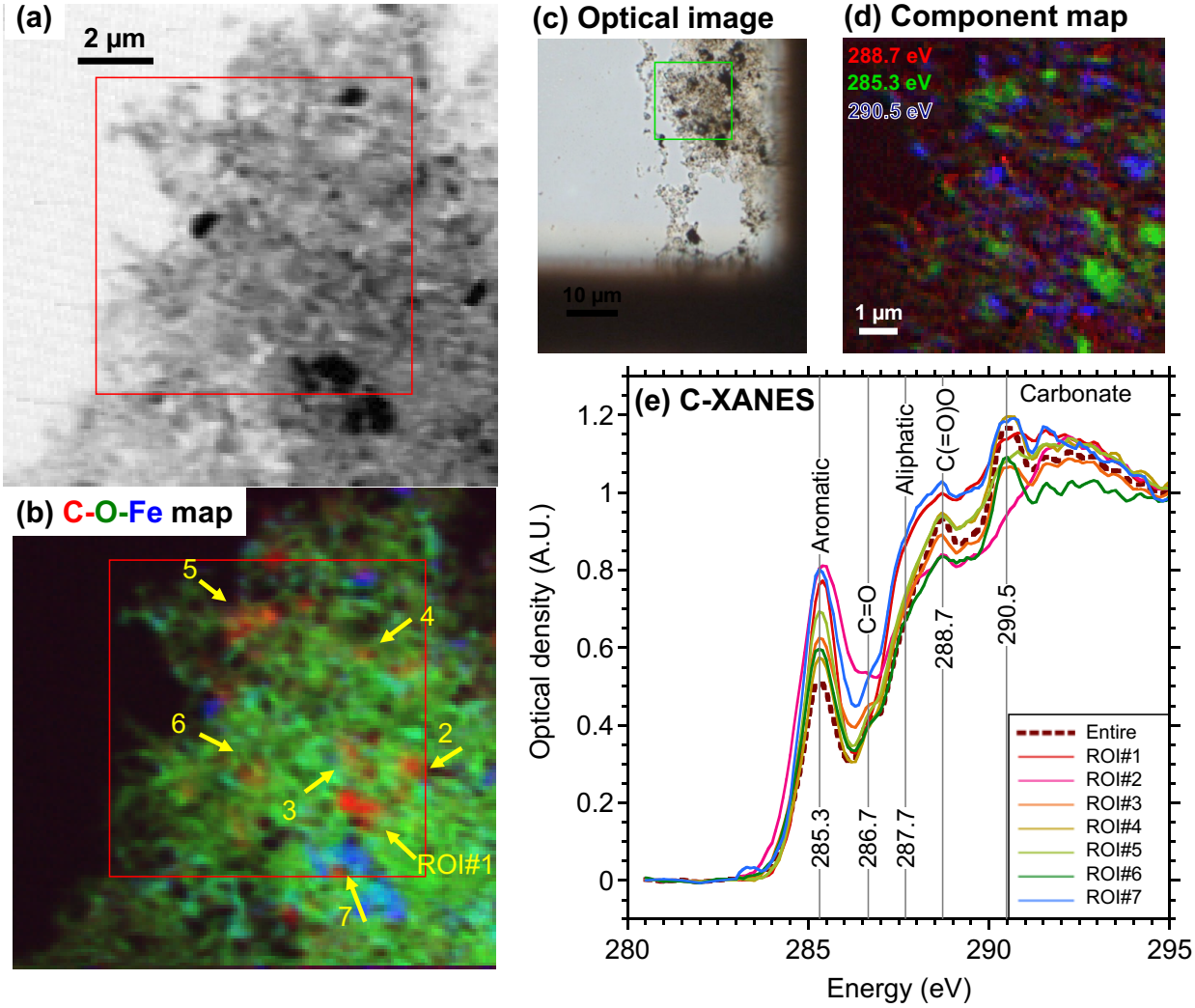

Fig. 1. (a) X-ray absorption image at 525 eV of the ultramicrotomed slice of the Zag clast. (b) carbon (in red) – oxygen (in green) – iron (in blue) map generated from STXM/XANES elemental maps, with ROI numbers indicated in yellow. (c) Optical microscopic image. (d) Compositional map generated by the stack data from the red squared region, at energies of 288.7 eV (C(=O)O, in red), 285.3 eV (aromatic C=C, in green) and 290.5 eV (CO_3, in blue). (e) C-XANES spectra from the red square entire region, and from the ROIs indicated by arrows in b).

3.2. SR-μFTIR, AFM-IR, Raman, and NanoSIMS

Conventional synchrotron μFTIR spectra of the ultramicrotomed slice shows peaks at ~1740 cm^{-1}, ~1500 cm^{-1}, and 1020 cm^{-1} corresponding to carbonyl (C=O), carbonates (CO_3 mode), and silicate Si-O, respectively (**Fig. 2f, lower curve**). We display in **Fig. 2** AFM-IR maps recorded at these fixed wavenumbers and combined to obtain a composite three-color image at high spatial resolution (**Fig. 2c**). In addition, a line of spectra crossing the ultramicrotomed sample, covering the full AFM-IR laser spectral span, was recorded. The integrated AFM-IR signal for the different bands retrieved from the analysis of this spectral line map is shown in **Fig. 2e**. Three individual AFM-IR spectra extracted in regions of high contrast at small spatial scale are also shown in **Fig. 2f**. These spectra show two important features: (i) AFM-IR data are in agreement with the conventional FTIR spectrum for the spatially widespread and intense bands, (ii) They sample variations of the individual bands at much higher spatial resolution, allowing measurement, for example, of the extent of at least four individual carbonates grains with (sub-)micron sizes, which would be inaccessible with conventional μFTIR. As shown in the organics composite image in **Fig. 2g**, this spectral line crosses a region of interest with high C=O and less C=C contribution than the lower part of the slice. The intrinsically lower band strength in the FTIR of the C=C absorption band can be however seen locally in the AFM-IR spectrum of #2 in **Fig. f**. At the global scale recorded FTIR spectrum, this FTIR C=C contribution appears as minor because the spectrum of the entire slice is largely dominated by the intense carbonyl, carbonate and silicates bands. The AFM-IR map is consistent to the STXM map in **Fig. 1d**, but the large organic particles were not observed in the STXM. The large organic particle could be lost in the section for STXM (there is a large void in the section as shown in **Fig. 1c** lower right), or the large particle was not hit in the slice used for STXM due to up to several hundreds of nm differences (equivalent to the thickness of several ultramicrotomed slices) of the sampling positions between the slices for STXM and AFM-IR.

The Raman fluorescence map is indicative of a change of nature of the underlying organics. The absolute level of fluorescence will strongly depend on the numerical aperture on the sample. The map of **Fig. 2d** was obtained by integrating the recorded Raman signal in a 500 cm^{-1} wide spectral window (3500-3000 cm^{-1}), i.e., above the D and G Raman bands, and corresponding to

a window centered at about 540 nm. Raman composite image **Fig. 2d** shows an aromatic component is widespread even outside the much more concentrated and intense aromatic local C spots such as ROI#1 and 2 identified in **Fig. 1b** STXM/XANES elemental maps. Raman spectra of the Zag clast show typical carbonaceous features represented by a G-band at around 1600 cm^{-1} and a D-band at around 1350 cm^{-1} (**Fig. 3**). The intensity ratios (I_D/I_G) of the G and D bands are indicated in **Fig. 3**. The composite map generated with the AFM-IR data shows that the submicrometer distribution of organic matter in Zag clast is consistent with STXM/XANES maps (**Fig. 1b,d**). Note that the STXM/XANES analysis was done with ultramicrotomed sections from the same sample grain and adjacent to the ones used for the AFM-IR and NanoSIMS analyses.

For the isotopic data, as a result of the applied threshold on the H^- counts, only areas with sufficiently high H concentrations, i.e. with substantial hydrogen-rich organic matter, are indicated on the composite image displayed in **Fig. 2b**. The NanoSIMS D/H image reveals a large hot-spot zone of a few tens μm^2 with high D/H ratios, located in the lower middle of the grain. The AFM-IR map permits identification of a large organic grain with an intense carbonyl signature that precisely overlaps the D-rich hot-spot and visible fluorescence (lower middle in **Fig. 2b,c,d**). This large D-rich organic grain has a δD value of (4200-4500)‰ while the δD of the surroundings and the main part of the sample is ~(1000-1100)‰. The D/H ratios of both the hot-spot and bulk are in agreement with the isotopic analysis reported in previous studies on the same clast from Zag (Kebukawa et al., 2019a; Kebukawa et al., 2020). The D-rich organic grain is associated with high Raman fluorescence clearly visible on **Fig. 2d**. In this zone the carbonyl signal is high, whereas the C=C is low (**Fig. 2g**), suggesting abundant aliphatic organic moieties more susceptible to fluorescence. The high fluorescence nature shown by Raman typically indicates enrichment of double bonds but each aromatic domain must be small (Bertrand et al., 1986). There is a C=O rich particle on the middle of **Fig. 2**, which also shows high fluorescence**.** The area on the left of the D-rich zone is dominated by aromatics with less C=O groups (**Fig. 2g**). The area on the right of the D-rich zone is dominated by diffuse organic matter together with a local concentration in form of organic particles (**Fig. 2c,g**).

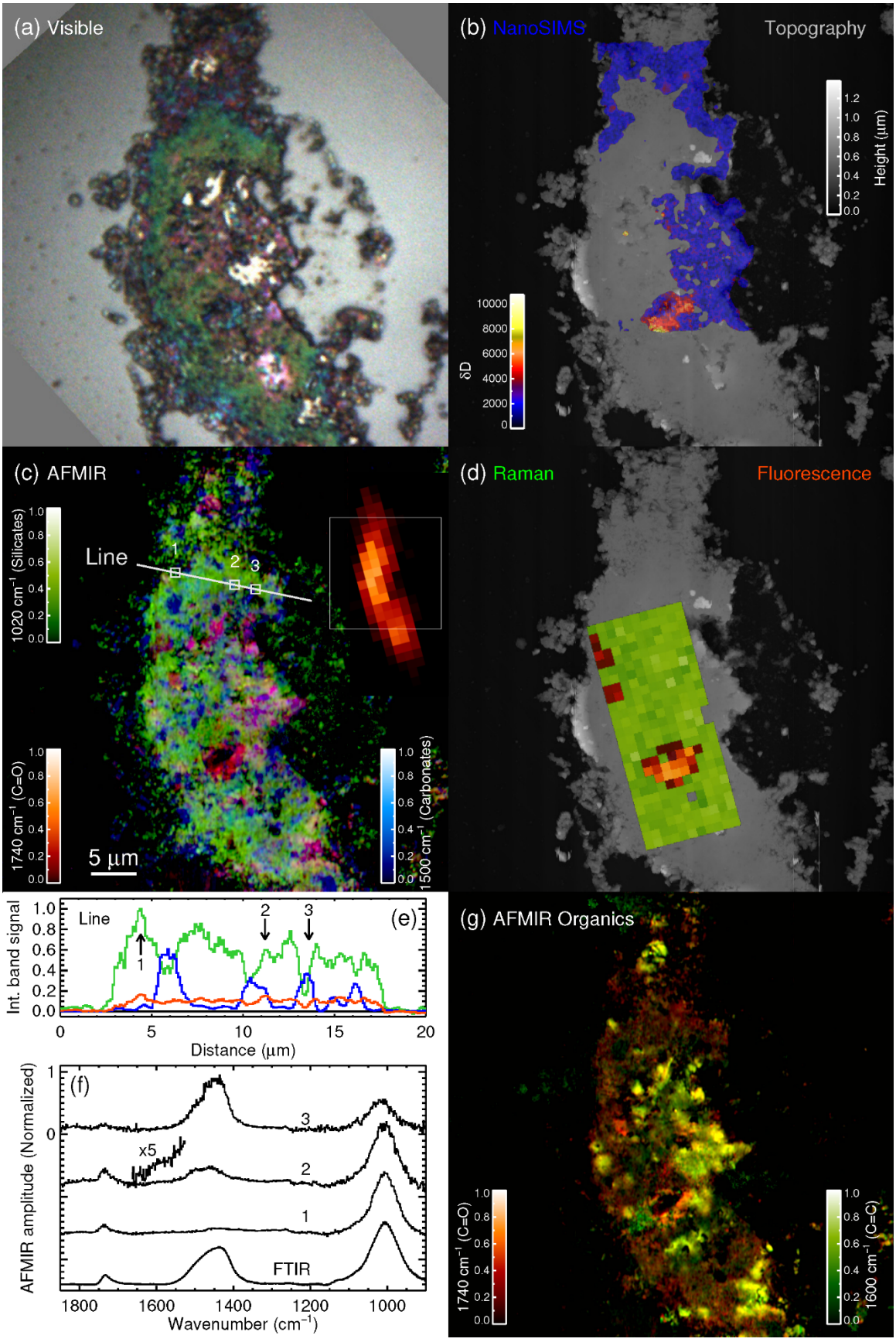
(a) Visible
(b) NanoSIMS
Topography
Height (µm)
δD
(c) AFMIR
Line
1020 cm⁻¹ (Silicates)
1740 cm⁻¹ (C=O)
1500 cm⁻¹ (Carbonates)
5 µm
(d) Raman
Fluorescence
(e)
Int. band signal
Distance (µm)
(f)
AFMIR amplitude (Normalized)
x5
FTIR
Wavenumber (cm⁻¹)
(g) AFMIR Organics
1740 cm⁻¹ (C=O)
1600 cm⁻¹ (C=C)

Fig. 2. Panel of images showing: (a) visible optical reflection image; (b) NanoSIMS δD image (in colors) overlaid on AFM topography (grey scale); (c) AFM-IR composite RGB map combining normalized AFM-IR maps recorded at 1740 cm^{-1} (carbonyl), 1500 cm^{-1} (carbonates), 1020 cm^{-1} (silicates), position of a spectra line map, and insert of the optimized µFTIR synchrotron map in the 1740 cm^{-1} carbonyl band; (d) Raman I_D/I_G map (green scale) and fluorescence (red scale) overlaid over the AFM topography map (grey scale); (e) AFM-IR line map obtained by integrating the three main band amplitudes (C=O in red at 1740 cm^{-1}, carbonates in blue at 1500 cm^{-1}, silicates in green at 1020 cm^{-1}) and (f) three spectra extracted from the line (e) showing the compositional diversity at the sub µm scale. The lowest spectrum is a conventional IR spectrum of the entire ultramicrotomed slice; (g) AFM-IR two color composite image focusing on the vibrational groups of organics at 1740 cm^{-1} (C=O, red) and 1600 cm^{-1} (C=C, green).

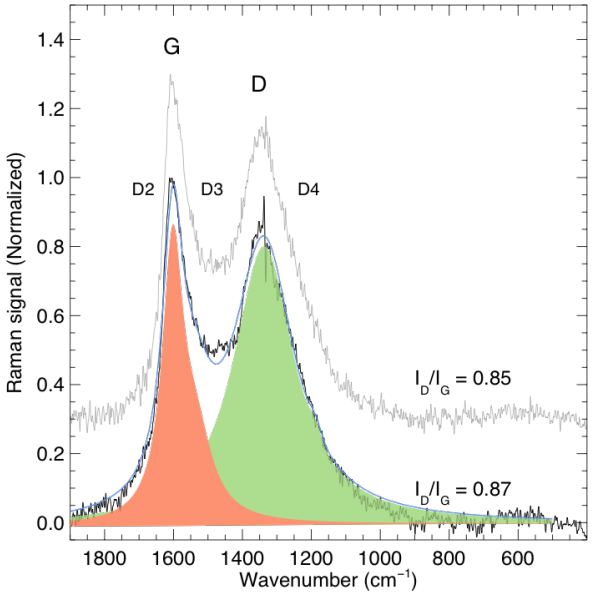

Fig 3. (lower curve) Average Raman spectrum over the entire map of **Fig. 2d**, excluding the fluorescence dominated regions (normalized to the maximum), deconvolved in D and G bands. (upper curve) The best S/N individual spectrum.

3.3. Mineralogy of the Zag clast

The mineralogy of the Zag clast was previously investigated by SEM-EDS, EPMA and TEM analyses (Zolensky et al., 2003; Fries et al., 2013). The clast is predominantly a fine-grained matrix, consisting of a mixture of serpentine, saponite, magnetite, Ca phosphates, organic-dominated grains, and pyrrhotite with exsolved pentlandite. Set within the matrix are larger aggregates of saponite, serpentine phases, magnetite, pyrrhotite/pentlandite, dolomite and halite/sylvite crystals. The largest observed dolomite aggregate has very interesting zoning: Mn-rich cores, carbonate, and very thin Na-Mg-rich rims. The Na-rich rims of these dolomites suggest a link between this clast and the scattered halite/sylvite xenoliths in Zag. EDS and EPMA measurements of phyllosilicate composition (**Fig. 4**) indicate intergrown serpentine and saponite, with a composition typical of CI, CM and CR carbonaceous chondrites. These identifications were verified by TEM observations. The clast appears to be homogeneous in mineralogy, as far as can be observed by SEM-BSE observation.

TEM observation of the ultrathin sections of four fragments from the clast shows that they are composed mainly of phyllosilicates containing abundant Fe-Ni sulfides (pyrrhotite $Fe_{1-x}S$ and pentlandite $(Fe,Ni)_9S_8$), magnetite Fe_3O_4, Mg-Fe carbonate $(Mg,Fe)CO_3$, and dolomite $CaMg(CO_3)_2$ (**Figs. 5 and 6a-d**). High-resolution TEM images of phyllosilicates indicate that the phyllosilicates are predominantly composed of saponite (**Figs. 5c, d**), which means that the four fragments were obtained from the areas that contained mainly saponite as phyllosilicates. Therefore, major chemical compositions of the phyllosilicates in the two fragments are plotted along the saponite solid solution line (**Fig. 7a**), which is consistent with the TEM observation (**Figs. 5c, d**). Their predominantly saponite-rich compositions are similar to those of phyllosilicates in hydrated fine-grained Antarctic micrometeorites (AMMs) and chondritic smooth interplanetary dust particles (CS IDPs) (Noguchi et al., 2002; Nakamura et al., 2004; Sakamoto et al., 2010; Dobrică et al., 2019), as well as coarse-grained phyllosilicates in the carbonate-rich lithology of the Tagish Lake ungrouped C2 chondrite (Nakamura et al., 2003). In addition, we found magnesiochromite $MgCr_2O_4$ (**Fig. 6e**), which was reported from CI chondrites (Rubin and Ma, 2021).

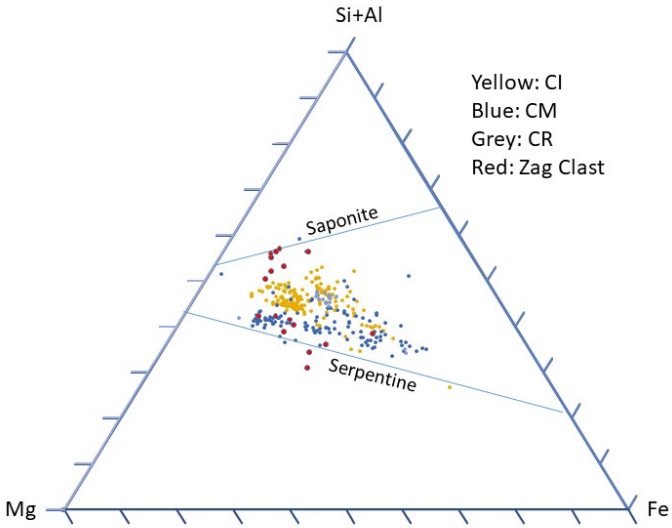

Fig. 4. Atomic % triangular diagram comparing bulk composition of phyllosilicates (essentially mixtures of serpentine family phases and saponite) in the Zag clast with matrix of CI, CM and CR chondrites. Note that there are some measurements of essentially pure aggregates of saponite and some of serpentine. Because the solid solution lines of saponite and serpentine shown in this diagram are actual mineral compositions rather than ideal ones, the lines are slanted rather than horizontal.

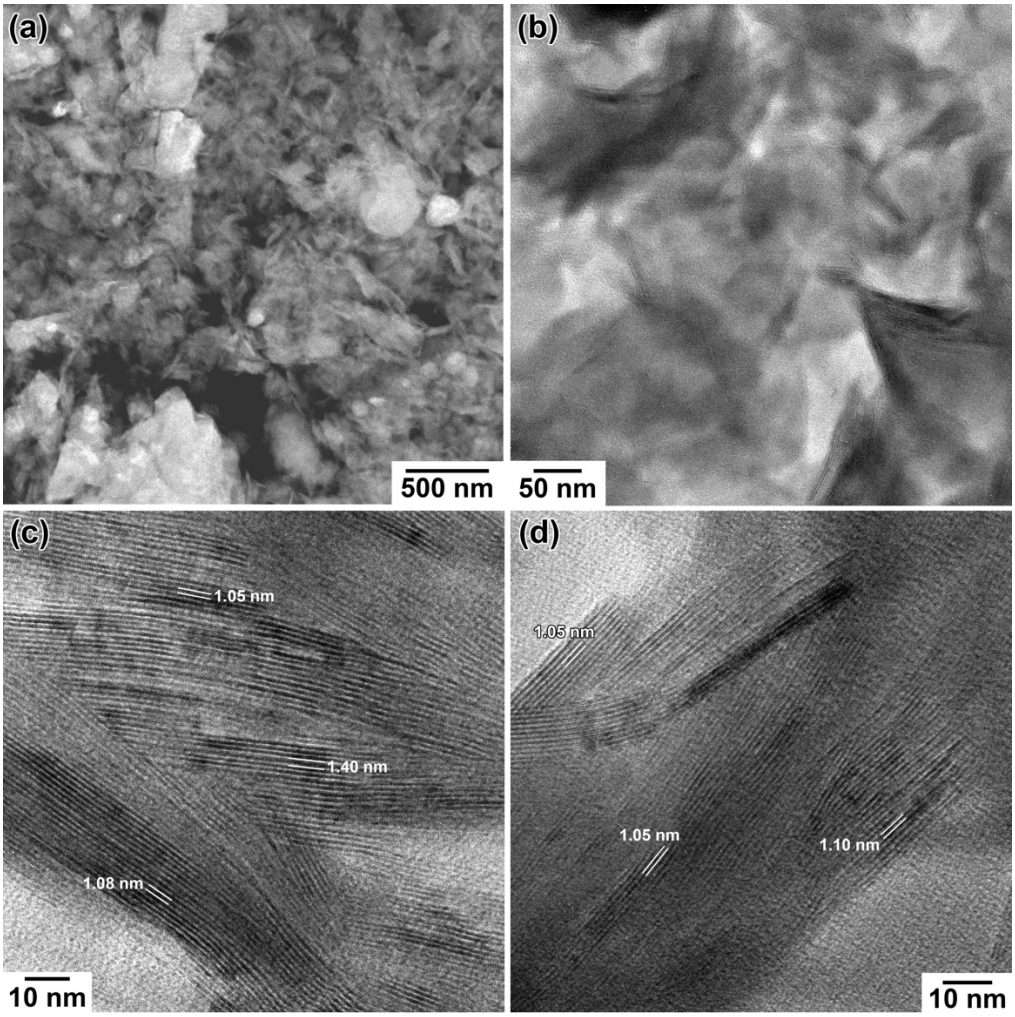

Fig. 5. TEM images of mineral phases in the Zag clast. (a) Low magnification high-angle annular dark-field – scanning transmission electron microscope (HAADF–STEM) image of the clast. It is composed mainly of fibrous phyllosilicates embedding Fe-Ni sulfides and Mg-Fe carbonate. (b) Bright-field (BF) TEM image of phyllosilicates. (c and d) High-resolution BF-TEM images show that the phyllosilicates are composed of saponite.

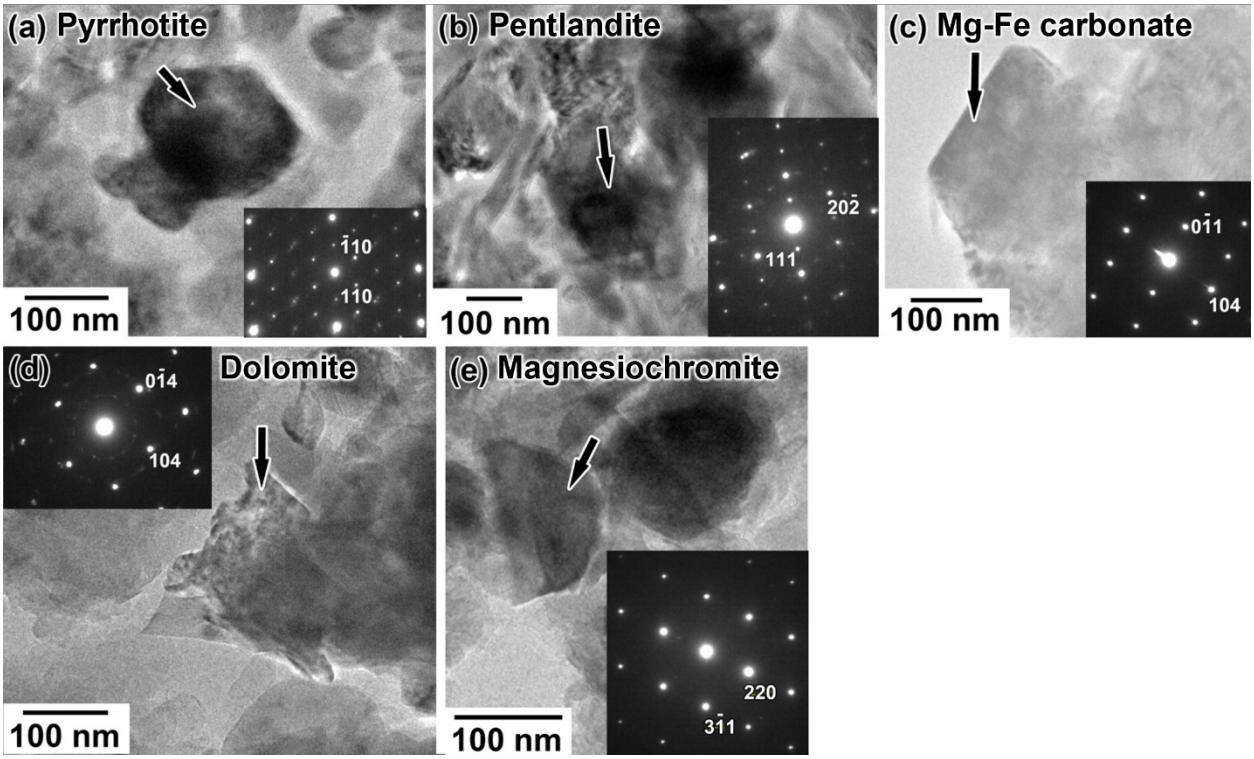

412

413 **Fig. 6.** TEM images of minerals and their selected area electron diffraction (SAED) patterns in

414 the clast. (a) Pyrrhotite. (b) Pentlandite. (c) Mg-Fe carbonate. (d) Dolomite. (e)

415 Magnesiochromite.

416

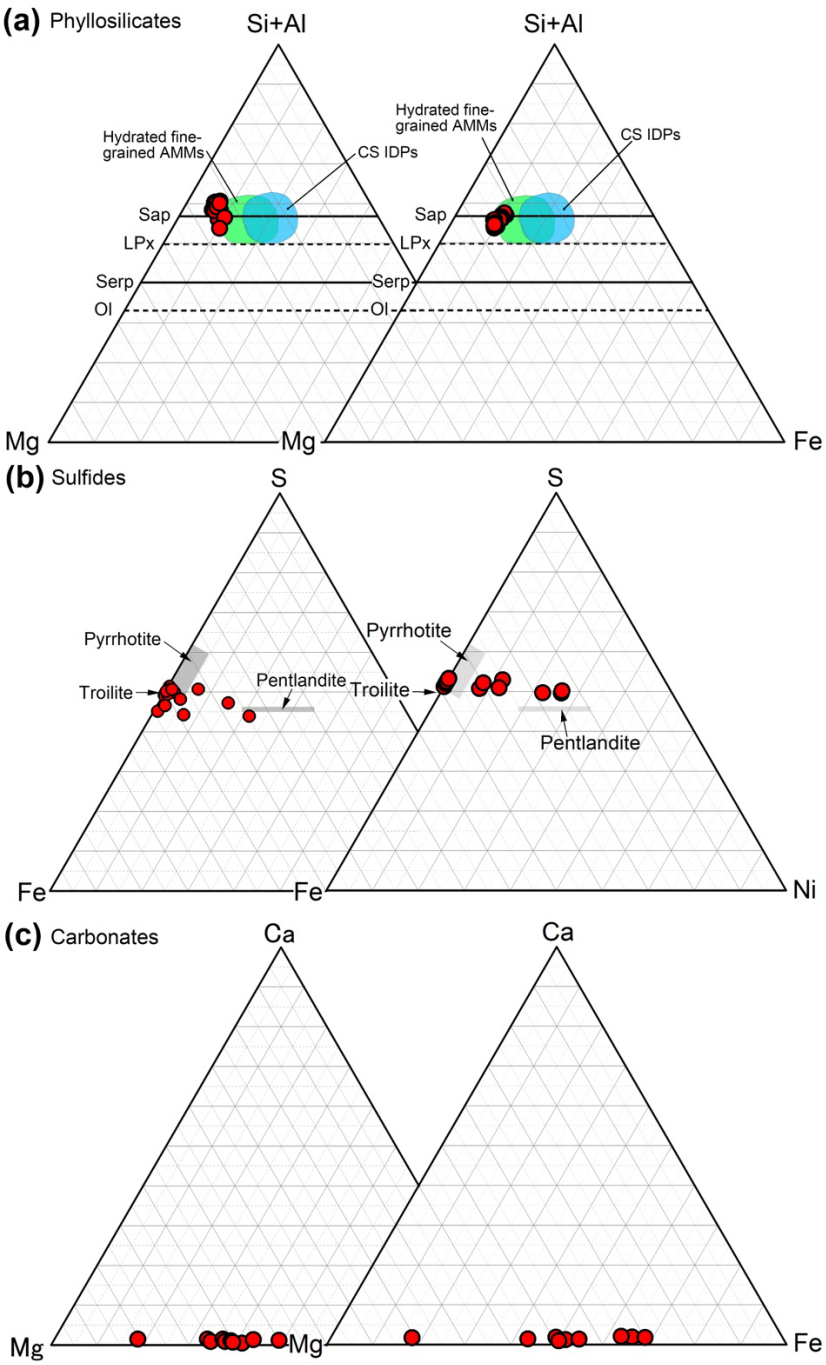

Fig. 7. Major chemical compositions of phyllosilicates, sulfides, and carbonates in the two fragments from the Zag clast. (a) [Si+Al]-Mg-Fe atomic ratios of phyllosilicates. Compositional fields of phyllosilicates in hydrated fine-grained AMMs and CS IDPs are from Noguchi et al. (2002), Nakamura et al. (2004), Sakamoto et al. (2010), and Dobrică et al. (2019). Because the solid solution lines of saponite and serpentine in these diagrams are ideal stoichiometric ones, they are parallel rather than slanted. (b) S-Fe-Ni atomic ratios of Fe-Ni sulfides in the clast. (c)

Ca-Mg-Fe atomic ratios of carbonates in the clast. Sap: saponite, LPx: low-Ca pyroxene, Serp: serpentine, and Ol: olivine.

4. Discussion: Origins of organic matter in the Zag clast

The organics in the Zag clast appear in two different forms as shown by STXM/XANES, AFM-IR, Raman and NanoSIMS: i) deuterium-rich, C=O rich with likely smaller aromatic domains, and ii) less deuterium-rich, relatively aromatic-rich with likely larger aromatic domains. Both types of organics have various shapes and size ranges from sub-μm up to a few μm. The latter would correspond to the "individual particles" in carbonaceous chondrites reported by Le Guillou et al. (2014) using STXM. These two forms should have different origins and/or alteration processes since their molecular structures and D/H ratios are different. The former was likely produced in relatively oxidized environments from D-rich precursors. Such organic particles could be formed during aqueous processing by hydrophobic aggregation (Cody et al., 2011; Kebukawa et al., 2013), from D-rich precursors from cold interstellar/outer solar nebulae (e.g., Mumma and Charnley, 2011) or in the ionizing region of the Solar System (Remusat et al., 2006; Gourier et al., 2008; Laurent et al., 2015). The other possibility is photosynthesis of the icy dust particles in interstellar/outer solar nebulae (e.g., Muñoz Caro and Dartois, 2013). Such icy dust could retain organic refractory materials after warming up in the solar nebula or planetesimals.

The latter, less deuterium-rich and aromatic-rich organics were likely produced in relatively reduced and higher temperature environments with less deuterium-enriched precursors, possibly in the inner Solar System. Fischer-Tropsch type (FTT) synthesis could have occurred at higher temperature regions in the nebula or in larger bodies (e.g., Anders et al., 1973; Kress and Tielens, 2001; Sekine et al., 2006; Nuth et al., 2008). Fischer-Tropsch synthesis intrinsically produces hydrocarbons from CO and H_2 gases with a catalyst, but further processing could form aromatic materials. Also, one cannot exclude the possibility of the contribution of carbonaceous materials from plasmatic environments around evolved stars (e.g., Sakata et al., 1983; Kwok, 2004; Endo et al., 2021). However, the FTT products are expected to have lower D/H ratios than the observed values (~1000‰), since the D/H ratio of H_2 in nebular gas was ~2.1×10^{-5} (−865‰)

(Geiss and Gloeckler, 1998). Such high D/H of aromatic-rich organics can be explained by the following two possibilities; (1) D-H exchange with H_2D^+ in a highly ionized region of the protoplanetary disk (Remusat et al., 2006; Gourier et al., 2008), and/or (2) D-H exchange with D-rich water in the parent body of the clast (Kebukawa et al. 2019a), whereas D-H exchange is slow at low temperatures enough to keep heterogeneities in D/H ratios (Kebukawa et al. 2021a).

Such mixtures of organics with various origins imply a complex mixing history in the protoplanetary disk before accretion of the original parent body of the Zag clast, involving materials from various heliocentric locations (Remusat et al., 2010). In any cases, aqueous alteration in the clast parent body overwrote isotopic and molecular structure information of the original materials and thus it is difficult to precisely constrain the formation scenarios.

Large condensed organic particles around 5 micrometers in diameter (such as shown in **Fig. 2c**) are rare in chondrites. Such large condensed organic particles were only reported in QUE 99177 (CR2) (Alexander et al., 2017), other than from the previous studies of the Zag clast (Kebukawa et al. 2019, 2020). Some micrometeorites recovered from Antarctic snow exhibit large organic matter concentrations, so called ultracarbonaceous Antarctic micrometeorites (UCAMMs) (Duprat et al., 2010; Dobrică et al., 2012; Dartois et al., 2013; Yabuta et al., 2017; Dartois et al., 2018). In addition, an UCAMM-like clast was found in the LAP 02342 CR2 chondrite (Nittler et al., 2019). The UCAMMs are often rich in nitrogen and deuterium (Duprat et al. 2010; Dartois et al. 2013, 2018), although it is not always the case (Yabuta et al. 2017) as there must exist a distribution in organic rich meteorite compositions. Unfortunately, the nitrogen abundance is not known in our sample. A notable difference between UCAMMs and the Zag clast are hydrated minerals. Hydrated minerals such as phyllosilicates and carbonates were not found in UCAMMs (Dobrică et al., 2012; Yabuta et al., 2017). Meanwhile, the Zag clast contains abundant phyllosilicates and carbonates (**Figs. 4, 5**) which require aqueous alteration. Organic matter and carbonates are likely embedded in the phyllosilicate matrix (**Figs. 1, 2**). Close association of organic matter and carbonate minerals implies water-organic-mineral interactions (Chan et al., 2017). In the case of the Tagish Lake meteorite, which is similar to the Zag clast, carbon isotopes indicate that the main carbon source of carbonates was not organic matter (Fujiya et al., 2019). Thus, the carbonates and organic matter in the Zag clast could have precipitated simultaneously,

but from different precursors; an aqueous fluid rich in CO_2 (Fujiya et al., 2019) and some other purely organic precursors (Cody et al., 2011), respectively. In this scenario, the D/H ratios of water and organic precursor must have been high, i.e., close to the current δD values of the diffused organic matter (~1000-1100 ‰), due to the significant D/H exchange between water and organic precursors (Kebukawa et al., 2021a).

The mineralogy of the clast has mineralogical heterogeneity. Some areas have mineralogy most similar to CIs. However, in some areas its mineralogy is more similar to CS IDPs and hydrated fine-grained AMMs. The chemistry and isotopic signatures of the clast suggest that the mineralogy of the clast is intermediate between these meteorites, IDPs, and AMMs. Usually, such fragile materials cannot reach the Earth as meteorites, e.g., CIs and Tagish Lake can be easily disassembled with a light poking. There are only 9 CI chondrites recorded to date, and the Tagish Lake meteorite is a very rare case—the only other similar one is the Tarda meteorite (Marrocchi et al., 2021). In the case of the clast, such fragile materials were gently incorporated into the regolith of the ordinary chondrite parent body and protected during atmospheric entry to the Earth. The observed mixture of the clast parent body within the host parent body required some degree of induration of the implanted projectile. However, the fact that halite survived in this clast (Rubin et al., 2002; Zolensky et al., 2017), along with organic nanoglobules, hydrous phyllosilicates, and other fragile materials, requires that it was not significantly processed by shock or heating during incorporation into the ordinary chondrite host. There may well have originally been much more of the clast material that was significantly processed during this incorporation event, and which has not survived in an intact form. Impact shock among asteroids is an extremely heterogeneous process (Stöffler et al., 1991), and thus it is not surprising that some material escaped significant processing.

The population of CI-like clasts is smaller than CM-like clasts in chondrite meteorite breccias which may be attributable to the friable nature of CI-like clasts, as well as CI-like material is destroyed preferentially during regolith gardening (Brearley and Prinz, 1992). Meanwhile, Patzek et al. (2018) showed that CI-like clasts occur all the studied brecciated meteorites including polymict ureilites, HEDs, CR, CB, CH, and ordinary chondrites, whereas the CM-like clasts have only been identified in HEDs and ordinary chondrites. There are many hydrated,

517 relatively unshocked clasts in H-chondrite regolith breccias (Rubin and Bottke, 2009). Raman
518 spectroscopic thermometer indicated that CI-like and CM-like clasts in polymict ureilites,
519 polymict eucrites, and howardite showed that the peak temperatures experienced by most of
520 these clasts were among the unheated CI and CM chondrites, but some clasts experienced
521 slightly higher temperatures > 100 °C. Nakashima et al. (2003) reported that the peripheries of
522 the CI-like clasts in the Tsukuba H chondrite were heated to 700 °C, while the interior of the
523 clasts has never experienced heating above 500 °C, indicating frictional heating between the
524 clasts and the host minerals. The Zag clast in our study showed no evidence of shock nor
525 heating, it is probably due to the large size of the clast where the inside could be protected from
526 heating. Rubin et al. (2002) suggested that the dark clasts in Zag formed from light-colored clasts
527 during shock events that melted and mobilized a significant fraction of their metallic Fe-Ni and
528 troilite grains. However, it is not the case of the clast studied here.
529
530 Rubin and Bottke (2009) implied that a moderate amount of ejecta was produced by the shock
531 events affected H chondrites 250–325 Ma ago and 3.4–4.1 Ga ago, the earlier event was
532 consistent with Nice Model (Levison et al. 2009). One can speculate that the Zag clast was
533 incorporated to regolith of a thermal-metamorphosed planetesimal with a low velocity impact,
534 perhaps 3.4–4.1 Ga ago allowing enough time to cool down the planetesimal from ^{26}Al-induced
535 heating. Then after lithification, and possibly after destruction of the original planetesimal and
536 reaccretion, the Zag meteorite was ejected from the H chondrite parent body, perhaps 250–325
537 Ma ago. Briani et al. (2012) also suggested that xenoliths and microxenoliths could have been
538 embedded in the H chondrite parent body earlier than 3 Ga ago, from the zodiacal cloud. Large
539 size (a few cm) of the Zag clast is not consistent with the dust size range of 10-100 μm in the
540 zodiacal cloud (Grogan et al. 2001), but the size cannot completely exclude the possibility of the
541 zodiacal could origin.
542
543 **5. Conclusions**
544
545 We performed AFM-IR and NanoSIMS coordinated analyses in addition to STXM/C-XANES,
546 Raman, TEM, and synchrotron μFTIR on a xenolithic carbonaceous clast from the Zag ordinary
547 chondrite. The mineralogy of this clast shown by (S)TEM shares more features more in common

with hydrated fine-grained AMMs and CS IDPs, rather than with CI chondrites and the Tagish Lake C2 ungrouped meteorite. We found two types of organics; i) deuterium-rich, C=O rich likely with smaller aromatic domains, probably produced by relatively oxidized environments from D-rich precursors, and ii) less deuterium-rich, aromatic-rich organics, maybe produced in relatively reduced and higher temperature environments, i.e., suitable for FTT synthesis, with less deuterium-enriched precursors, possibly the inner Solar System. Both types of organics have various shapes and size ranges from sub-µm up to a few µm. Such mixtures of organics with various origins imply a complex mixing history involving materials from various heliocentric locations before accretion of the original parent body of the Zag clast. If this parent body was an aqueously altered D/P-type asteroid (Kebukawa et al. 2019, 2020), our findings support the idea of a wide heliocentric mixture of materials in the early Solar System (Bockelée–Morvan et al., 2002; Ciesla and Dullemond, 2010; Remusat et al., 2010; Brownlee, 2014).

Notably, we demonstrated the feasibility of successful coordinated analyses with AFM-IR, Raman and NanoSIMS on the very same area of the sample allowed by the sulfur-embedded ultramicrotoming technique which enabled production of several consecutive thin sections from the same particle. The capability to perform coupled AFM-IR and NanoSIMS analysis on the very same subsample permits for the first time comparison of the isotopic signature of sub-µm components identified by their IR signatures. Moreover, STXM/C-XANES was performed on adjacent, the nearly-identical ultramicrotomed slices with the AFM-IR. We showed that the distributions of the organic matter in AFM-IR map and STXM/XANES map were consistent, but also complementary, since STXM/XANES is more sensitive to aromatics than AFM-IR but cannot detect silicates. Such technical advantages are critical for the characterization of precious astromaterials including asteroidal regolith samples returned to Earth by the Hayabusa2 (Yabuta et al. 2022 submitted) and OSIRIS-REx spacecraft.

Acknowledgments

Y.K. was supported by Japan Society for the Promotion of Science KAKENHI (grant number JP17H06458 and JP19H05073). We thank travel support from the Core2disk program at Université Paris Saclay. T.N. was supported by JSPS KAKENHI Grant Numbers 19H00725 and

19KK0094. M.Z. was supported by the NASA Emerging Worlds Program. J.D. thanks the Région Ile de France for funding via the DIM-ACAV+ project C3E. L.R. thanks the European Research Council for funding via the ERC project HYDROMA (grant agreement No. 819587). The NanoSIMS facility in Paris was established by funds from the CNRS, Région Ile de France, Ministère délégué à l'Enseignement Supérieur et à la Recherche, and the Muséum National d'Histoire Naturelle. We acknowledge SOLEIL for provision of synchrotron radiation facilities in using beamline SMIS. The AFM-IR studies were funded by CNES (MIAMI2) and ANR (COMETOR ANR-18-CE31-0011). We thank Richard Norton for donating the Zag clast to us.

References

Alexander, C.M.O.D., Cody, G.D., De Gregorio, B.T., Nittler, L.R., Stroud, R.M., 2017. The nature, origin and modification of insoluble organic matter in chondrites, the major source of Earth's C and N. Chemie der Erde Geochemistry 77, 227-256, 10.1016/j.chemer.2017.01.007

Anders, E., Hayatsu, R., Studier, M.H., 1973. Organic compounds in meteorites. Science 182, 781-790, 10.1126/science.182.4114.781

Bardin, N., Duprat, J., Slodzian, G., Wu, T.-D., Baklouti, D., Dartois, E., Brunetto, R., Engrand, C., Guerquin-Kern, J.-L., 2015. Hydrogen isotopic fractionation in secondary ion mass spectrometry using polyatomic ions. Int. J. Mass spectrom. 393, 17-24, 10.1016/j.ijms.2015.10.005

Bertrand, P., Pittion, J.-L., Bernaud, C., 1986. Fluorescence of sedimentary organic matter in relation to its chemical composition. Org. Geochem. 10, 641-647, 10.1016/0146-6380(86)90061-6

Bockelée–Morvan, D., Gautier, D., Hersant, F., Huré, J.-M., Robert, F., 2002. Turbulent radial mixing in the solar nebula as the source of crystalline silicates in comets. A&A 384, 1107-1118

Bonal, L., Huss, G.R., Krot, A.N., Nagashima, K., 2010a. Chondritic lithic clasts in the CB/CH-like meteorite Isheyevo: Fragments of previously unsampled parent bodies. Geochim. Cosmochim. Acta 74, 2500-2522, 10.1016/j.gca.2010.01.029

Bonal, L., Huss, G.R., Krot, A.N., Nagashima, K., Ishii, H.A., Bradley, J.P., 2010b. Highly ^{15}N-enriched chondritic clasts in the CB/CH-like meteorite Isheyevo. Geochim. Cosmochim. Acta 74, 6590-6609, 10.1016/j.gca.2010.08.017

Brearley, A.J., 1990. Carbon-rich aggregates in type 3 ordinary chondrites: Characterization, origins, and thermal history. Geochim. Cosmochim. Acta 54, 831-850, 10.1016/0016-7037(90)90377-W

Brearley, A.J., Prinz, m., 1992. CI chondrite-like clasts in the Nilpena polymict ureilite: Implications for aqueous alteration processes in CI chondrites. Geochim. Cosmochim. Acta 56, 1373-1386, 10.1016/0016-7037(92)90068-T

Briani, G., Gounelle, M., Bourot-Denise, M., Zolensky, M.E., 2012. Xenoliths and microxenoliths in H chondrites: Sampling the zodiacal cloud in the asteroid Main Belt. Meteoritics & Planetary Science 47, 880-902, https://doi.org/10.1111/j.1945-5100.2012.01367.x

Briani, G., Gounelle, M., Marrocchi, Y., Mostefaoui, S., Leroux, H., Quirico, E., Meibom, A., 2009. Pristine extraterrestrial material with unprecedented nitrogen isotopic variation. Proceedings of the National Academy of Sciences of the United States of America 106, 10522-10527, 10.1073/pnas.0901546106

Brownlee, D., 2014. The Stardust Mission: Analyzing samples from the edge of the solar system. Annual Review of Earth and Planetary Sciences 42, 179-205, 10.1146/annurev-earth-050212-124203

Chan, Q.H.S., Zolensky, M.E., Bodnar, R.J., Farley, C., Cheung, J.C.H., 2017. Investigation of organo-carbonate associations in carbonaceous chondrites by Raman spectroscopy. Geochim. Cosmochim. Acta 201, 392-409, 10.1016/j.gca.2016.10.048

Ciesla, F.J., Dullemond, C.P., 2010. Evolution of protoplanetary disk structures, in: Lauretta, D.S., Apai, D. (Eds.), Protoplanetary Dust: Astrophysical and Cosmochemical Perspectives. Cambridge University Press, Cambridge, pp. 66-96.

Cody, G.D., Ade, H., Alexander, C.M.O., Araki, T., Butterworth, A., Fleckenstein, H., Flynn, G., Gilles, M.K., Jacobsen, C., Kilcoyne, A.L.D., Messenger, K., Sandford, S.A., Tyliszczak, T., Westphal, A.J., Wirick, S., Yabuta, H., 2008. Quantitative organic and light-element analysis of comet 81P/Wild 2 particles using C-, N-, and O-μ-XANES. Meteoritics & Planetary Science 43, 353-365, 10.1111/j.1945-5100.2008.tb00627.x

Cody, G.D., Heying, E., Alexander, C.M.O.D., Nittler, L.R., Kilcoyne, A.L.D., Sandford, S.A., Stroud, R.M., 2011. Establishing a molecular relationship between chondritic and cometary organic solids. Proc. Natl. Acad. Sci. U. S. A. 108, 19171-19176, 10.1073/pnas.1015913108

Dartois, E., Engrand, C., Brunetto, R., Duprat, J., Pino, T., Quirico, E., Remusat, L., Bardin, N., Briani, G., Mostefaoui, S., Morinaud, G., Crane, B., Szwec, N., Delauche, L., Jamme, F., Sandt, C., Dumas, P., 2013. UltraCarbonaceous Antarctic micrometeorites, probing the Solar System beyond the nitrogen snow-line. Icarus 224, 243-252, 10.1016/j.icarus.2013.03.002

Dartois, E., Engrand, C., Duprat, J., Godard, M., Charon, E., Delauche, L., Sandt, C., Borondics, F., 2018. Dome C ultracarbonaceous Antarctic micrometeorites. A&A 609, A65, 10.1051/0004-6361/201731322

Dazzi, A., Prazeres, R., Glotin, F., Ortega, J.M., 2005. Local infrared microspectroscopy with subwavelength spatial resolution with an atomic force microscope tip used as a photothermal sensor. Opt. Lett. 30, 2388-2390, 10.1364/OL.30.002388

De Gregorio, B.T., Stroud, R.M., Cody, G.D., Nittler, L.R., Kilcoyne, A.L.D., Wirick, S., 2011. Correlated microanalysis of cometary organic grains returned by Stardust. Meteoritics & Planetary Science 46, 1376-1396, 10.1111/j.1945-5100.2011.01237.x

De Gregorio, B.T., Stroud, R.M., Nittler, L.R., Alexander, C.M.O.D., Bassim, N.D., Cody, G.D., Kilcoyne, A.L.D., Sandford, S.A., Milam, S.N., Nuevo, M., Zega, T.J., 2013. Isotopic and chemical variation of organic nanoglobules in primitive meteorites. Meteoritics & Planetary Science 48, 904-928, 10.1111/maps.12109

De Gregorio, B.T., Stroud, R.M., Nittler, L.R., Alexander, C.M.O.D., Kilcoyne, A.L.D., Zega, T.J., 2010. Isotopic anomalies in organic nanoglobules from Comet 81P/Wild 2: Comparison to Murchison nanoglobules and isotopic anomalies induced in terrestrial organics by electron irradiation. Geochim. Cosmochim. Acta 74, 4454-4470, 10.1016/j.gca.2010.05.010

Dobrică, E., Engrand, C., Leroux, H., Rouzaud, J.N., Duprat, J., 2012. Transmission Electron Microscopy of CONCORDIA UltraCarbonaceous Antarctic MicroMeteorites (UCAMMs): Mineralogical properties. Geochim. Cosmochim. Acta 76, 68-82, 10.1016/j.gca.2011.10.025

Dobrică, E., Ogliore, R.C., Engrand, C., Nagashima, K., Brearley, A.J., 2019. Mineralogy and oxygen isotope systematics of magnetite grains and a magnetite-dolomite assemblage in hydrated fine-grained Antarctic micrometeorites. Meteoritics & Planetary Science 54, 1973-1989, 10.1111/maps.13366

Dominguez, G., McLeod, A.S., Gainsforth, Z., Kelly, P., Bechtel, H.A., Keilmann, F., Westphal, A., Thiemens, M., Basov, D.N., 2014. Nanoscale infrared spectroscopy as a non-destructive probe of extraterrestrial samples. Nature Communications 5, 10.1038/ncomms6445

Duprat, J., Dobrica, E., Engrand, C., Aleon, J., Marrocchi, Y., Mostefaoui, S., Meibom, A., Leroux, H., Rouzaud, J.N., Gounelle, M., Robert, F., 2010. Extreme deuterium excesses in ultracarbonaceous micrometeorites from central Antarctic snow. Science 328, 742-745, 10.1126/science.1184832

Endo, I., Sakon, I., Onaka, T., Kimura, Y., Kimura, S., Wada, S., Helton, L.A., Lau, R.M., Kebukawa, Y., Muramatsu, Y., Ogawa, N.O., Ohkouchi, N., Nakamura, M., Kwok, S., 2021. On the Nature of Organic Dust in Novae. The Astrophysical Journal 917, 103, 10.3847/1538-4357/ac0cf1

Fries, M., Messenger, S., Steele, A., Zolensky, M., 2013. Do We Already have Samples of Ceres? H Chondrite Halites and the Ceres-Hebe Link. 76th Annual Meeting of the Meteoritical Society, Abstract #5266

Fujiya, W., Hoppe, P., Ushikubo, T., Fukuda, K., Lindgren, P., Lee, M.R., Koike, M., Shirai, K., Sano, Y., 2019. Migration of D-type asteroids from the outer Solar System inferred from carbonate in meteorites. Nature Astronomy 3, 910-915, 10.1038/s41550-019-0801-4

Geiss, J., Gloeckler, G., 1998. Abundances of Deuterium and Helium-3 in the Protosolar Cloud. Space Science Reviews 84, 239-250, 10.1023/A:1005039822524

Gounelle, M., Zolensky, M.E., Liou, J.-C., Bland, P.A., Alard, O., 2003. Mineralogy of carbonaceous chondritic microclasts in howardites: identification of C2 fossil micrometeorites. Geochim. Cosmochim. Acta 67, 507-527, 10.1016/S0016-7037(02)00985-7

Gourier, D., Robert, F., Delpoux, O., Binet, L., Vezin, H., Moissette, A., Derenne, S., 2008. Extreme deuterium enrichment of organic radicals in the Orgueil meteorite: Revisiting the interstellar interpretation? Geochim. Cosmochim. Acta 72, 1914-1923, 10.1016/j.gca.2008.01.017

Grogan, K., Dermott, S.F., Durda, D.D., 2001. The Size–Frequency Distribution of the Zodiacal Cloud: Evidence from the Solar System Dust Bands. Icarus 152, 251-267, https://doi.org/10.1006/icar.2001.6638

703 Kebukawa, Y., Ito, M., Zolensky, M.E., Greenwood, R.C., Rahman, Z., Suga, H., Nakato, A., Chan,
704 Q.H., Fries, M., Takeichi, Y., 2019a. A novel organic-rich meteoritic clast from the outer
705 solar system. Scientific Reports 9, 3169, 10.1038/s41598-019-39357-1
706 Kebukawa, Y., Kilcoyne, A.L.D., Cody, G.D., 2013. Exploring the potential formation of organic
707 solids in chondrites and comets through polymerization of interstellar formaldehyde.
708 Astrophys. J. 771, 19, 10.1088/0004-637x/771/1/19
709 Kebukawa, Y., Kobayashi, H., Urayama, N., Baden, N., Kondo, M., Zolensky, M.E., Kobayashi, K.,
710 2019b. Nanoscale infrared imaging analysis of carbonaceous chondrites to understand
711 organic-mineral interactions during aqueous alteration. Proceedings of the National
712 Academy of Sciences 116, 753-758, 10.1073/pnas.1816265116
713 Kebukawa, Y., Kobayashi, S., Kawasaki, N., Wang, Y., Yurimoto, H., Cody, G.D., 2021a. Hydrogen
714 isotopic exchange kinetics between organic matter and water: Implications for chemical
715 evolution during meteorite parent body processing. Meteoritics & Planetary Science 56,
716 440-454, 10.1111/maps.13629
717 Kebukawa, Y., Zolensky, M.E., Chan, Q.H.S., Nagao, K., Kilcoyne, A.L.D., Bodnar, R.J., Farley, C.,
718 Rahman, Z., Le, L., Cody, G.D., 2017. Characterization of carbonaceous matter in
719 xenolithic clasts from the Sharps (H3.4) meteorite: Constraints on the origin and thermal
720 processing. Geochim. Cosmochim. Acta 196, 74-101, 10.1016/j.gca.2016.09.024
721 Kebukawa, Y., Zolensky, M.E., Goodrich, C.A., Ito, M., Ogawa, N.O., Takano, Y., Ohkouchi, N.,
722 Kiryu, K., Igisu, M., Shibuya, T., Marcus, M.A., Ohigashi, T., Martinez, J., Kodama, Y.,
723 Shaddad, M.H., Jenniskens, P., 2021b. Organic matter in carbonaceous chondrite
724 lithologies of Almahata Sitta: Incorporation of previously unsampled carbonaceous
725 chondrite lithologies into ureilitic regolith. Meteoritics & Planetary Science 56, 1311-
726 1327, 10.1111/maps.13713
727 Kebukawa, Y., Zolensky, M.E., Ito, M., Ogawa, N.O., Takano, Y., Ohkouchi, N., Nakato, A., Suga,
728 H., Takeichi, Y., Takahashi, Y., Kobayashi, K., 2020. Primordial organic matter in the
729 xenolithic clast in the Zag H chondrite: Possible relation to D/P asteroids. Geochim.
730 Cosmochim. Acta 271, 61-77, 10.1016/j.gca.2019.12.012
731 Kouketsu, Y., Mizukami, T., Mori, H., Endo, S., Aoya, M., Hara, H., Nakamura, D., Wallis, S., 2014.
732 A new approach to develop the Raman carbonaceous material geothermometer for low-
733 grade metamorphism using peak width. Island Arc 23, 33-50, 10.1111/iar.12057
734 Kress, M.E., Tielens, A., 2001. The role of Fischer-Tropsch catalysis in solar nebula chemistry.
735 Meteoritics & Planetary Science 36, 75-91, 10.1111/j.1945-5100.2001.tb01811.x
736 Kwok, S., 2004. The synthesis of organic and inorganic compounds in evolved stars. Nature 430,
737 985-991, 10.1038/nature02862
738 Laurent, B., Roskosz, M., Remusat, L., Robert, F., Leroux, H., Vezin, H., Depecker, C., Nuns, N.,
739 Lefebvre, J.-M., 2015. The deuterium/hydrogen distribution in chondritic organic matter
740 attests to early ionizing irradiation. Nature Communications 6, 8567,
741 10.1038/ncomms9567
742 Le Guillou, C., Bernard, S., Brearley, A.J., Remusat, L., 2014. Evolution of organic matter in
743 Orgueil, Murchison and Renazzo during parent body aqueous alteration: In situ
744 investigations. Geochim. Cosmochim. Acta 131, 368-392, 10.1016/j.gca.2013.11.020

745 Levison, H.F., Bottke, W.F., Gounelle, M., Morbidelli, A., Nesvorny, D., Tsiganis, K., 2009.
746 Contamination of the asteroid belt by primordial trans-Neptunian objects. Nature 460,
747 364-366, 10.1038/nature08094
748 Marrocchi, Y., Avice, G., Barrat, J.-A., 2021. The Tarda Meteorite: A Window into the Formation
749 of D-type Asteroids. The Astrophysical Journal Letters 913, L9, 10.3847/2041-
750 8213/abfaa3
751 Mathurin, J., Dartois, E., Pino, T., Engrand, C., Duprat, J., Deniset-Besseau, A., Borondics, F.,
752 Sandt, C., Dazzi, A., 2019. Nanometre-scale infrared chemical imaging of organic matter
753 in ultra-carbonaceous Antarctic micrometeorites (UCAMMs). Astronomy & Astrophysics
754 622, A160, 10.1051/0004-6361/201833957
755 Mathurin, J., Deniset-Besseau, A., Dazzi, A., 2020. Advanced Infrared Nanospectroscopy Using
756 Photothermal Induced Resonance Technique, AFMIR: New Approach Using Tapping
757 Mode. Acta Physica Polonica, A. 137
758 Muñoz Caro, G.M., Dartois, E., 2013. Prebiotic chemistry in icy grain mantles in space. An
759 experimental and observational approach. Chem. Soc. Rev. 42, 2173-2185,
760 10.1039/c2cs35425j
761 Mumma, M.J., Charnley, S.B., 2011. The chemical composition of comets-emerging taxonomies
762 and natal heritage. Annual Review of Astronomy and Astrophysics 49, 471-524,
763 10.1146/annurev-astro-081309-130811
764 Nakamura, K., Keller, L.P., Nakamura, T., Noguchi, T., Zolensky, M.E., 2004. Mineralogical Study
765 of Hydrated IDPs: X-Ray Diffraction and Transmission Electron Microscopy, Lunar and
766 Planetary Science Conference, p. 1862.
767 Nakamura, T., Noguchi, T., Zolensky, M.E., Tanaka, M., 2003. Mineralogy and noble-gas
768 signatures of the carbonate-rich lithology of the Tagish Lake carbonaceous chondrite:
769 evidence for an accretionary breccia. Earth. Planet. Sci. Lett. 207, 83-101,
770 10.1016/s0012-821x(02)01127-5
771 Nakashima, D., Nakamura, T., Noguchi, T., 2003. Formation history of CI-like phyllosilicate-rich
772 clasts in the Tsukuba meteorite inferred from mineralogy and noble gas signatures.
773 Earth. Planet. Sci. Lett. 212, 321-336
774 Nittler, L.R., Stroud, R.M., Trigo-Rodríguez, J.M., De Gregorio, B.T., Alexander, C.M.O.D.,
775 Davidson, J., Moyano-Cambero, C.E., Tanbakouei, S., 2019. A cometary building block in
776 a primitive asteroidal meteorite. Nature Astronomy 3, 659-666, 10.1038/s41550-019-
777 0737-8
778 Noguchi, T., Nakamura, T., Nozaki, W., 2002. Mineralogy of phyllosilicate-rich micrometeorites
779 and comparison with Tagish Lake and Sayama meteorites. Earth. Planet. Sci. Lett. 202,
780 229-246, 10.1016/s0012-821x(02)00777-x
781 Noguchi, T., Takase, M., Matsumoto, R., Kebukawa, Y., Suga, H., Kondo, M., Takahashi, Y.,
782 Takeichi, Y., Yabuta, H., 2020. An another protocol to make sulfur embedded ultrathin
783 sections of extraterrestrial small samples. Life 10, 135, 10.3390/life10080135
784 Noguchi, T., Yabuta, H., Itoh, S., Sakamoto, N., Mitsunari, T., Okubo, A., Okazaki, R., Nakamura,
785 T., Tachibana, S., Terada, K., Ebihara, M., Imae, N., Kimura, M., Nagahara, H., 2017.
786 Variation of mineralogy and organic material during the early stages of aqueous activity
787 recorded in Antarctic micrometeorites. Geochim. Cosmochim. Acta 208, 119-144,
788 10.1016/j.gca.2017.03.034

789 Nuth, J.A., III, Johnson, N.M., Manning, S., 2008. A self-perpetuating catalyst for the production
790 of complex organic molecules in protostellar nebulae. Astrophysical Journal Letters 673,
791 L225-L228, 10.1086/528741
792 Patzek, M., Bischoff, A., Visser, R., John, T., 2018. Mineralogy of volatile-rich clasts in brecciated
793 meteorites. Meteoritics & Planetary Science 53, 2519-2540,
794 https://doi.org/10.1111/maps.13175
795 Patzek, M., Hoppe, P., Bischoff, A., Visser, R., John, T., 2020. Hydrogen isotopic composition of
796 CI- and CM-like clasts from meteorite breccias – Sampling unknown sources of
797 carbonaceous chondrite materials. Geochim. Cosmochim. Acta 272, 177-197,
798 https://doi.org/10.1016/j.gca.2019.12.017
799 Phan, V.T.H., Rebois, R., Beck, P., Quirico, E., Bonal, L., Noguchi, T., 2022. Nanoscale mineralogy
800 and organic structure in Orgueil (CI) and EET 92042 (CR) carbonaceous chondrites
801 studied with AFM-IR spectroscopy. Meteoritics & Planetary Science 57, 3-21,
802 10.1111/maps.13773
803 Remusat, L., Guan, Y., Wang, Y., Eiler, J.M., 2010. Accretion and preservation of D-rich organic
804 particles in carbonaceous chondrites: Evidence for important transport in the early solar
805 system nebula. The Astrophysical Journal 713, 1048-1058, 10.1088/0004-
806 637x/713/2/1048
807 Remusat, L., Palhol, F., Robert, F., Derenne, S., France-Lanord, C., 2006. Enrichment of
808 deuterium in insoluble organic matter from primitive meteorites: A solar system origin?
809 Earth. Planet. Sci. Lett. 243, 15-25, 10.1016/j.epsl.2005.12.010
810 Rubin, A., Ma, C., 2021. Meteorite Mineralogy. Cambridge University Press, pp.404.
811 Rubin, A.E., Bottke, W.F., 2009. On the origin of shocked and unshocked CM clasts in H-
812 chondrite regolith breccias. Meteoritics & Planetary Science 44, 701-724,
813 https://doi.org/10.1111/j.1945-5100.2009.tb00764.x
814 Rubin, A.E., Zolensky, M.E., Bodnar, R.J., 2002. The halite‐bearing Zag and Monahans (1998)
815 meteorite breccias: Shock metamorphism, thermal metamorphism and aqueous
816 alteration on the H‐chondrite parent body. Meteoritics & Planetary Science 37, 125-
817 141
818 Sadezky, A., Muckenhuber, H., Grothe, H., Niessner, R., Pöschl, U., 2005. Raman
819 microspectroscopy of soot and related carbonaceous materials: Spectral analysis and
820 structural information. Carbon 43, 1731-1742,
821 https://doi.org/10.1016/j.carbon.2005.02.018
822 Sakamoto, K., Nakamura, T., Noguchi, T., Tsuchiyama, A., 2010. A new variant of saponite-rich
823 micrometeorites recovered from recent Antarctic snowfall. Meteoritics & Planetary
824 Science 45, 220-237, 10.1111/j.1945-5100.2010.01019.x
825 Sakata, A., Wada, S., Okutsu, Y., Shintani, H., Nakada, Y., 1983. Does a 2,200 Å hump observed
826 in an artificial carbonaceous composite account for UV interstellar extinction? Nature
827 301, 493-494, 10.1038/301493a0
828 Sekine, Y., Sugita, S., Shido, T., Yamamoto, T., Iwasawa, Y., Kadono, T., Matsui, T., 2006. An
829 experimental study on Fischer-Tropsch catalysis: Implications for impact phenomena
830 and nebular chemistry. Meteoritics & Planetary Science 41, 715-729, 10.1111/j.1945-
831 5100.2006.tb00987.x

Stöffler, D., Keil, K., Edward R.D, S., 1991. Shock metamorphism of ordinary chondrites. Geochim. Cosmochim. Acta 55, 3845-3867, 10.1016/0016-7037(91)90078-J

Takeichi, Y., Inami, N., Suga, H., Miyamoto, C., Ueno, T., Mase, K., Takahashi, Y., Ono, K., 2016. Design and performance of a compact scanning transmission X-ray microscope at the Photon Factory. Rev. Sci. Instrum. 87, 013704

Vinogradoff, V., Le Guillou, C., Bernard, S., Binet, L., Cartigny, P., Brearley, A.J., Remusat, L., 2017. Paris vs. Murchison: Impact of hydrothermal alteration on organic matter in CM chondrites. Geochim. Cosmochim. Acta 212, 234-252, 10.1016/j.gca.2017.06.009

Watanabe, M., Williams, D.B., 2006. The quantitative analysis of thin specimens: a review of progress from the Cliff-Lorimer to the new ζ-factor methods. Journal of Microscopy 221, 89-109, 10.1111/j.1365-2818.2006.01549.x

Yabuta, H., Noguchi, T., Itoh, S., Nakamura, T., Miyake, A., Tsujimoto, S., Ohashi, N., Sakamoto, N., Hashiguchi, M., Abe, K.-i., Okubo, A., Kilcoyne, A.L.D., Tachibana, S., Okazaki, R., Terada, K., Ebihara, M., Nagahara, H., 2017. Formation of an ultracarbonaceous Antarctic micrometeorite through minimal aqueous alteration in a small porous icy body. Geochim. Cosmochim. Acta 214, 172-190, 10.1016/j.gca.2017.06.047

Yesiltas, M., Glotch, T.D., Kaya, M., 2021. Nanoscale Infrared Characterization of Dark Clasts and Fine-Grained Rims in CM2 Chondrites: Aguas Zarcas and Jbilet Winselwan. ACS Earth and Space Chemistry 5, 3281-3296, 10.1021/acsearthspacechem.1c00290

Young, J.M., Glotch, T.D., Yesiltas, M., Hamilton, V.E., Breitenfeld, L.B., Bechtel, H.A., Corder, S.N.G., Yao, Z., 2022. Nano-FTIR Investigation of the CM Chondrite Allan Hills 83100. Journal of Geophysical Research: Planets 127, e2021JE007166, 10.1029/2021JE007166

Zolensky, M., Clayton, R., Mayeda, T., Chokai, J., Norton, O., 2003. Carbonaceous chondrite clasts in the halite-bearing H5 chondrite Zag. Meteoritics and Planetary Science Supplement 38

Zolensky, M., Hewins, R., Mittlefehldt, D., Lindstrom, M., Xiao, X., Lipschutz, M., 1992. Mineralogy, petrology and geochemistry of carbonaceous chondritic clasts in the LEW 85300 polymict eucrite. Meteoritics 27, 596-604

Zolensky, M.E., Bodnar, R.J., Yurimoto, H., Itoh, S., Fries, M., Steele, A., Chan, Q.H.-S., Tsuchiyama, A., Kebukawa, Y., Ito, M., 2017. The search for and analysis of direct samples of early Solar System aqueous fluids. Philosophical Transactions of the Royal Society A 375, 20150386, 10.1098/rsta.2015.0386

Zolensky, M.E., Weisberg, M.K., Buchanan, P.C., Mittlefehldt, D.W., 1996. Mineralogy of carbonaceous chondrite clasts in HED achondrites and the Moon. Meteoritics & Planetary Science 31, 518-537